Table 4.3.4.2. *Plasmon energies measured (and calculated) for a few simple metals; most data have been extracted from Raether (1980)*

Monovalent			Divalent			Trivalent			Tetravalent		
$\hbar\omega_p$ (eV)			$\hbar\omega_p$ (eV)			$\hbar\omega_p$ (eV)			$\hbar\omega_p$ (eV)		
	Meas.	Calc.		Meas.	Calc.		Meas.	Calc.		Meas.	Calc.
Li	7.1	(8.0)	Be	18.7	(18.4)	B	22.7	(?)	C	34.0	(31)
Na	5.7	(5.9)	Mg	10.4	(10.9)	Al	14.95	(15.8)	Si	16.5	(16.6)
K	3.7	(4.3)	Ca	8.8	(8.0)	Ga	13.8	(14.5)	Ge	16.0	(15.6)
Rb	3.4	(3.9)	Sr	8.0	(7.0)	In	11.4	(12.5)	Sn	13.7	(14.3)
Cs	2.9	(3.4)	Ba	7.2	(6.7)	Sc	14.0	(12.9)	Pb	(13)	(13.5)

solution, reproduced in Fig. 4.3.4.11, is due to Castaing & Henry (1962). It consists of a double magnetic prism and a concave electrostatic mirror biased at the potential of the microscope cathode. The system possesses two pairs of stigmatic points that may coincide with a diffraction plane and an image plane of the electron-microscope column. One of these sets of points is achromatic and can be used for image filtering. The other is strongly chromatic and is used for spectrum analysis. Zanchi, Sevely & Jouffrey (1977) and Rose & Plies (1974) have proposed replacing this system, which requires an extra source of high voltage for the mirror, by a purely magnetic equivalent device. Several solutions, known as the α and ω filters, with three or four magnets, have thus been built, both on very high voltage microscopes (Zanchi, Perez & Sevely, 1975) and on more conventional ones (Krahl & Herrmann, 1980), the latest version now being available from one EM manufacturer (Zeiss EM S12).

4.3.4.2.3. *Detection systems*

The final important component in EELS is the detector that measures the electron flux in the dispersion plane of the spectrometer and transfers it through a suitable interface to the data storage device for further computer processing. Until about 1990, all systems were operated in a sequential acquisition mode. The dispersed beam was scanned in front of a narrow slit located in the spectrometer dispersion plane. Electrons were then generally recorded by a combination of scintillator and photomultiplier capable of single electron counting.

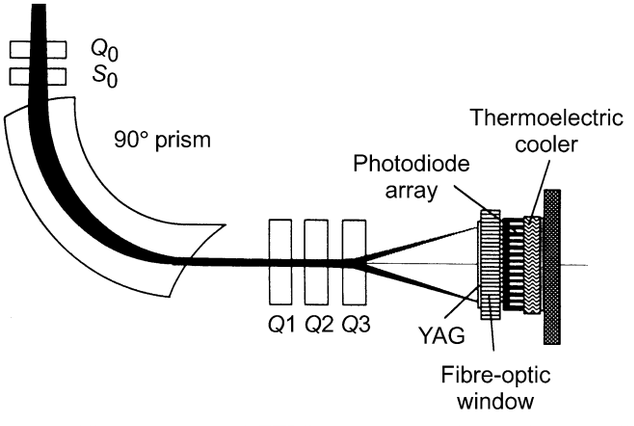

Fig. 4.3.4.12. A commercial EELS spectrometer designed for parallel detection on a photodiode array. The family of quadrupoles controls the dispersion on the detector level [courtesy of Krivanek *et al.* (1987))].

This process is, however, highly inefficient: while the counts are measured in one channel, all information concerning the other channels is lost. These requirements for improved detection efficiency have led to the consideration of possible solutions for parallel detection of the EELS spectrum. They use a multiarray of detectors, the position, the size and the number of which have to be adapted to the spectral distribution delivered by the spectrometer. In most cases with magnetic type devices, auxiliary electron optics has to be introduced between the spectrometer and the detector so that the dispersion matches the size of the individual detection cells. Different systems have been proposed and tested for recording media, the most widely used solutions at present being the photodiode and the charge-coupled diode arrays described by Shuman & Kruit (1985), Krivanek, Ahn & Keeney (1987), Strauss, Naday, Sherman & Zaluzec (1987), Egerton & Crozier (1987), Berger & McMullan (1989), *etc.* Fig. 4.3.4.12 shows a device, now commercially available from Gatan, that is made of a convenient combination of these different components. This progress in detection has led to significant improvements in many areas of EELS: enhanced detection limits, reduced beam damage in sensitive materials, data of improved quality in terms of both SNR and resolution, and access to time-resolved spectroscopy at the ms time scale (chronospectra). Several of these important consequences are illustrated in the following sections.

4.3.4.3. *Excitation spectrum of valence electrons*

Most inelastic interaction of fast incident electrons is with outer atomic shells in atoms, or in solids with valence electrons (referred to as conduction electrons in metals). These involve excitations in the 0–50 eV range, but, in a few cases, interband transitions from low-binding-energy shells may also contribute.

4.3.4.3.1. *Volume plasmons*

The basic concept introduced by the many-body theory in the interacting free electron gas is the volume plasmon. In a condensed material, the assembly of loosely bound electrons behaves as a plasma in which collective oscillations can be induced by a fast external charged particle. These eigenmodes, known as *volume plasmons*, are longitudinal charge-density fluctuations around the average bulk density in the plasma $n \simeq 10^{28}$ e^-/m^3). Their eigen frequency is given, in the free electron gas, as

$$\omega_p = \left(\frac{n e^2}{m\varepsilon_0}\right)^{1/2}. \qquad (4.3.4.8)$$

The corresponding $\hbar\omega_p$ energy, measured in an energy-loss spectrum (see the famous example of the plasmon in aluminium

Table 4.3.4.3. *Experimental and theoretical values for the coefficient α in the plasmon dispersion curve together with estimates of the cut-off wavevector (from Raether, 1980)*

	Measured α	Calculated α	q_c (Å^{-1})
Li	0.24	0.35	0.9
Na	0.24	0.32	0.8
K	0.14	0.29	0.8
Mg	0.35	0.39	1.0
Al	0.2 (<0.5 Å^{-1})		
	0.45 (>0.5 Å^{-1})	0.43	1.3
In	0.40 (<0.5 Å^{-1})		
	0.66 (>0.5 Å^{-1})		
Si	0.41		
	0.3	0.45	1.1

Table 4.3.4.4. *Comparison of measured and calculated values for the halfwidth $\Delta E_{1/2}(0)$ of the plasmon line (from Raether, 1980)*

	Experimental (eV)	Theory (eV)
Li	2.2	2.55
Na	0.3	0.12
K	0.25	0.15
Rb	0.6	0.64
Cs	1.2	0.96
Al	0.53	0.43
Mg	0.7	0.7
Si	3.2	5.4
Ge	3.1	3.9

in Fig. 4.3.4.3), is the *plasmon energy*, for which typical values in a selection of pure solid elements are gathered in Table 4.3.4.2. The accuracies of the measured values depend on several instrumental parameters. Moreover, they are sensitive to the specimen crystalline state and to its degree of purity. Consequently, there exist slight discrepancies between published values. Numbers listed in Table 4.3.4.2 must therefore be accepted with a 0.1 eV confidence. Some specific cases require comments: amorphous boron, when prepared by vacuum evaporation, is not a well defined specimen. Carbon exists in several allotropic varieties. The selection of the diamond type in the table is made for direct comparison with the other tetravalent specimens (Si, Ge, Sn). The results for lead (Pb) are still subject to confirmation. The volumic mass density is an important factor (through n) in governing the value of the plasmon energy. It varies with temperature and may be different in the crystal, in the amorphous, and in the liquid phases. In simple metals, the amorphous state is generally less dense than the crystalline one, so that its plasmon energy shifts to lower energies.

The above description applies only to very small scattering vectors $\mathbf{q}$. In fact, the plasmon energy increases with scattering angle (and with momentum transfer $\hbar\mathbf{q}$). This dependence is known as the dispersion relation, in which two distinct behaviours can be described:

(a) For small momentum transfers ($q \lesssim q_c$), the dispersion curve is parabolic:

$$\hbar\omega_p(q) = \hbar\omega_p(0) + \frac{\alpha\hbar^2}{m_0} q^2. \qquad (4.3.4.9)$$

The coefficient α has been measured in a number of substances and calculated for the free-electron case in the random phase approximation (Lindhard, 1954); see Table 4.3.4.3 for some data. A simple expression for α is

$$\alpha = \tfrac{3}{5}\frac{E_F}{\hbar\omega_p(0)}, \qquad (4.3.4.10)$$

where E_F is the Fermi energy of the electron gas. More detailed observations indicated that it is not possible to describe the dispersion curve over a large momentum range with a single q^2 law. In fact, one has to fit the experiment data with different linear or quadratic slopes as a function of q [see values indicated for Al and In in Table 4.3.4.3, and Hohberger, Otto & Petri (1975)]. Moreover, anisotropy has been found along different $\mathbf{q}$ directions in monocrystals (Manzke, 1980). In parallel, refinements have been brought into the calculations by including band-structure effects to deal with the anisotropy of the dispersion relation and with the bending of the experimental curves. Electron–electron correlations have also been considered, which has slightly improved the agreement between calculated and measured values of α (Bross, 1978*a*, *b*).

(b) For large momentum transfers, there exists a critical wavevector q_c, which corresponds to a strong decay of the plasmon mode into single electron–hole pair excitations. This can be calculated using conservation rules in energy and momentum, giving

$$\hbar\omega_p(0) + \alpha\frac{\hbar^2}{m_0} q_c^2 = \frac{\hbar^2}{2m_0}(q_c^2 + 2q_c q_F), \qquad (4.3.4.11)$$

where q_F is the Fermi wavevector. A simple approximation is $q_c \simeq \omega_p/v_F$, v_F being the Fermi velocity. Single pair excitations can be created by fast incoming electrons in the domain of scattering conditions contained between the two curves:

$$\left.\begin{aligned} \Delta E_{\max} &= \frac{\hbar^2}{2m_0}(q^2 + 2qq_F) \\ \Delta E_{\min} &= \frac{\hbar^2}{2m_0}(q^2 - 2qq_F) \end{aligned}\right\} \qquad (4.3.4.12)$$

shown in Fig. 4.3.4.13. They bracket the curve $\Delta E = \hbar^2 q^2/2m_0$ corresponding to the transfer of energy and momentum to an isolated free electron. For momentum transfers such as $q > q_c$, the plasmon mode is heavily damped and it is difficult to distinguish its own specific behaviour from the electron–hole continuum. A few studies, *e.g.* Batson & Silcox (1983), indicate that the plasmon dispersion curve flattens as it enters the

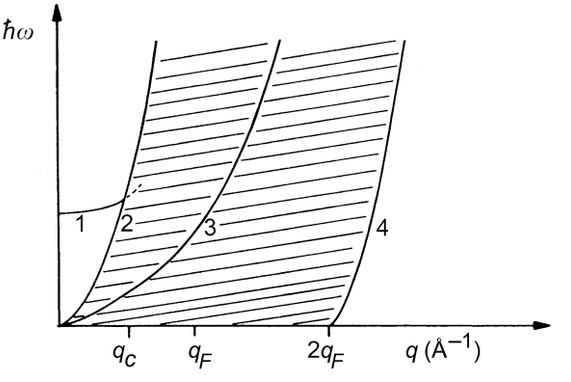

Fig. 4.3.4.13. The dispersion curve for the excitation of a plasmon (curve 1) merges into the continuum of individual electron–hole excitations (between curves 2 and 4) for a critical wavevector q_c. The intermediate curve (3) corresponds to Compton scattering on a free electron.

quasiparticle domain and approaches the centre of the continuum close to the free-electron curve. However, not only is the scatter between measurements fairly high, but a satisfactory theory is not yet available [see Schattschneider (1989) for a compilation of data on the subject].

Plasmon lifetime is inversely proportional to the energy width of the plasmon peak $\Delta E_{1/2}$. Even for Al, with one of the smallest plasmon energy widths ($\simeq 0.5$ eV), the lifetime is very short: after about five oscillations, their amplitude is reduced to $1/e$. Such a damping demonstrates the strength of the coupling of the collective modes with other processes. Several mechanisms compete for plasmon decay:

(*a*) For small momentum transfer, it is generally attributed to vertical interband transitions. Table 4.3.4.4, extracted from Raether (1980), compares a few measured values of $\Delta E_{1/2}(0)$, with values calculated using band-structure descriptions.

(*b*) For moderate momentum transfer q, a variation law such as

$$\Delta E_{1/2}(q) = \Delta E_{1/2}(0) + Bq^2 + O(q^4) \qquad (4.3.4.13)$$

has been measured. The q dependence of $\Delta E_{1/2}$ is mainly accounted for by non-vertical transitions compatible with the band structure, the number of these transitions increasing with q (Sturm, 1982). Other mechanisms have also been suggested, such as phonons, *umklapp* processes, scattering on surfaces, *etc*.

(*c*) For large momentum transfer (*i.e.* of the order of the critical wavevector q_c), the collective modes decay into the strong electron–hole-pair channels already described giving rise to a clear increase of the damping for values of $q > q_c$.

Within this free-electron-gas description, the differential cross section for the excitation of bulk plasmons by incident electrons of velocity v is given by

$$\frac{\mathrm{d}\sigma_p}{\mathrm{d}\Omega}(\theta) = \frac{\Delta E_p}{2\pi N a_0 m_0 v^2} \frac{1}{\theta^2 + \theta_E^2}, \qquad (4.3.4.14)$$

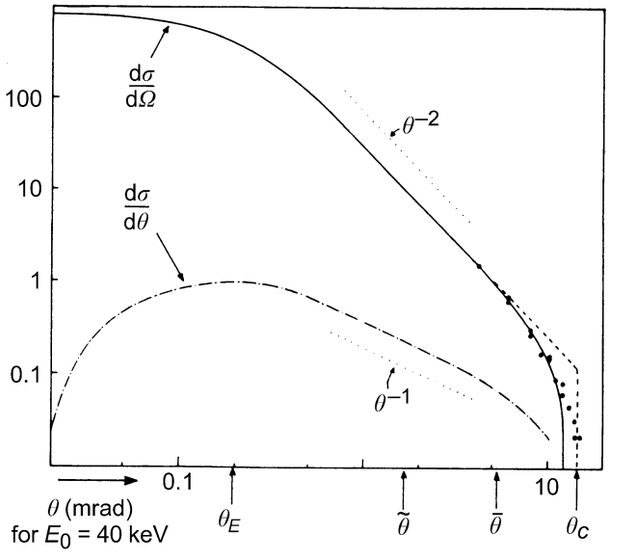

Fig. 4.3.4.14. Measured angular dependence of the differential cross section $\mathrm{d}\sigma/\mathrm{d}\Omega$ for the 15 eV plasmon loss in Al (dots) compared with a calculated curve by Ferrell (solid curve) and with a sharp cut-off approximation at θ_c (dashed curved). Also shown along the scattering angle axis, θ_E = characteristic inelastic angle defined as $\Delta E/2E_0$, $\tilde{\theta}$ = median inelastic angle defined by $\int_0^{\tilde{\theta}} (\mathrm{d}\sigma/\mathrm{d}\Omega)\,\mathrm{d}\Omega = 1/2 \int_0^{\theta_c} (\mathrm{d}\sigma/\mathrm{d}\Omega)\,\mathrm{d}\Omega$, and $\bar{\theta}$ = average inelastic angle defined by $\bar{\theta} = \int \theta(\mathrm{d}\sigma/\mathrm{d}\Omega)\,\mathrm{d}\Omega / \int (\mathrm{d}\sigma/\mathrm{d}\Omega)\,\mathrm{d}\Omega$ [courtesy of Egerton (1986)].

where N is the density of atoms per volume unit and θ_E is the characteristic inelastic angle defined as $\Delta E_p/2E_0$ in the non-relativistic description and as $\Delta E_p/\gamma m_0 v^2$ {with $\gamma = [1 - (v^2/c^2)]^{-1/2}$} in the relativistic case. The angular dependence of the differential cross section for plasmon scattering is shown in Fig. 4.3.4.14. The integral cross section up to an angle β_0 is

$$\sigma_p(\beta_0) = \int_0^{\beta_0} \left(\frac{\mathrm{d}\sigma_p}{\mathrm{d}\Omega}\right) \mathrm{d}\Omega = \frac{\Delta E_p \log(\beta_0/\theta_E)}{N a_0 m_0 v^2}. \qquad (4.3.4.15)$$

The total plasmon cross section is calculated for $\beta_0 = \theta_c = q_c/k_0$. Converted into mean free path, this becomes

$$\Lambda_p = \frac{1}{N\sigma_p} = \frac{a_0}{\theta_E} \left(\log \frac{\theta_c}{\theta_E}\right)^{-1} \quad \text{(non-relativistic formula);} \qquad (4.3.4.16)$$

and

$$\Lambda_p = \frac{a_0 \gamma m_0 v^2}{\Delta E_p} \left(\log \frac{\hbar q_c v}{1.132 \hbar \omega_p}\right)^{-1} \quad \text{(relativistic formula).} \qquad (4.3.4.17)$$

The behaviour of Λ_p as a function of the primary electron energy is shown in Fig. 4.3.4.15.

4.3.4.3.2. *Dielectric description*

The description of the bulk plasmon in the free-electron gas can be extended to any type of condensed material by introducing the dielectric response function $\varepsilon(\mathbf{q}, \omega)$, which describes the frequency and wavevector-dependent polarizability of the medium; *cf*. Daniels *et al* (1970). One associates, respectively, the ε_T and ε_L functions with the propagation of transverse and longitudinal EM modes through matter. In the small-$\mathbf{q}$ limit, these tend towards the same value:

$$\lim_{q\to 0} \varepsilon_T(\mathbf{q}, \omega) = \lim_{q\to 0} \varepsilon_L(\mathbf{q}, \omega) = \varepsilon(0, \omega).$$

As transverse dielectric functions are only used for wavevectors close to zero, the T and L indices can be omitted so that:

$$\varepsilon_L(\mathbf{q}, \omega) = \varepsilon(\mathbf{q}, \omega) \quad \text{and} \quad \varepsilon_T(\mathbf{q}, \omega) = \varepsilon(0, \omega).$$

The transverse solution corresponds to the normal propagation of EM waves in a medium of dielectric coefficient $\varepsilon(0, \omega)$, *i.e.* to

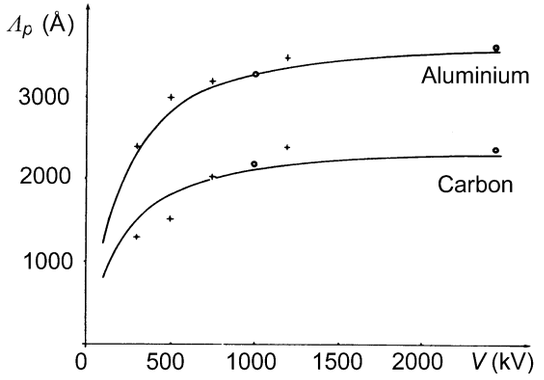

Fig. 4.3.4.15. Variation of plasmon excitation mean free path Λ_p as a function of accelerating voltage V in the case of carbon and aluminium [courtesy of Sevely (1985)].

$$\frac{q^2c^2}{\omega^2} - \varepsilon(0,\omega) = 0. \qquad (4.3.4.18)$$

For longitudinal fields, the only solution is $\varepsilon(\mathbf{q},\omega) = 0$, which is basically the dispersion relation for the bulk plasmon.

In the framework of the Maxwell description of wave propagation in matter, it has been shown by several authors [see, for instance, Ritchie (1957)] that the transfer of energy between the beam electron and the electrons in the solid is governed by the magnitude of the energy-loss function $-\mathrm{Im}[1/\varepsilon(\mathbf{q},\omega)]$, so that

$$\frac{\mathrm{d}^2\sigma}{\mathrm{d}(\Delta E)\,\mathrm{d}\Omega} = \frac{1}{N(e\pi a_0)^2}\,\frac{1}{q^2}\,\mathrm{Im}\left(-\frac{1}{\varepsilon(\mathbf{q},\omega)}\right). \qquad (4.3.4.19)$$

One can deduce (4.3.4.14) by introducing a δ function at energy loss ω_p for the energy-loss function:

$$\mathrm{Im}\left(-\frac{1}{\varepsilon(\mathbf{q},\omega)}\right) = \frac{\pi}{2}\,\omega_p\delta(\omega-\omega_p). \qquad (4.3.4.20)$$

As a consequence of the causality principle, a knowledge of the energy-loss function $-\mathrm{Im}[1/\varepsilon(\omega)]$ over the complete frequency (or energy-loss) range enables one to calculate $\mathrm{Re}[1/\varepsilon(\omega)]$ by Kramers–Kronig analysis:

$$\mathrm{Re}\frac{1}{\varepsilon(\omega)} = 1 - \frac{2}{\pi}\mathrm{PP}\int_0^\infty \mathrm{Im}\left(-\frac{1}{\varepsilon(\omega')}\right)\frac{\omega'}{\omega'^2-\omega^2}\,\mathrm{d}\omega', \qquad (4.3.4.21)$$

where PP denotes the principal part of the integral. For details of efficient practical evaluation of the above equation, see Johnson (1975).

The dielectric functions can be easily calculated for simple descriptions of the electron gas. In the Drude model, *i.e.* for a free-electron plasma with a relaxation time τ, the dielectric function at long wavelengths ($q \to 0$) is

$$\varepsilon(\omega) = \varepsilon_1(\omega) + i\varepsilon_2(\omega) = 1 - \frac{\omega_p^2}{\omega^2}\,\frac{1}{(1-1/i\omega\tau),} \qquad (4.3.4.22)$$

with $\omega_p^2 = ne^2/m\varepsilon_0$, as above. The behaviour of the different functions, the real and imaginary terms in ε, and the energy-loss function are shown in Fig. 4.3.4.16. The energy-loss term exhibits a sharp Lorentzian profile centred at $\omega = \omega_p$ and of width $1/\tau$. The narrower and more intense this plasmon peak, the more the involved valence electrons behave like free electrons.

In the Lorentz model, *i.e.* for a gas of bound electrons with one or several excitation eigenfrequencies ω_i, the dielectric function is

$$\varepsilon(\omega) = 1 + \sum_i \frac{n_i e^2}{m\varepsilon_0}\,\frac{1}{\omega_i^2 - \omega^2 + i\omega/\tau_i}, \qquad (4.3.4.23)$$

where n_i denotes the density of electrons oscillating with the frequency ω_i and τ_i is the associated relaxation time. The characteristic ε_1, ε_2, and $-\mathrm{Im}(1/\varepsilon)$ behaviours are displayed in Fig. 4.3.4.17: a typical 'interband' transition (in solid-state terminology) can be revealed as a maximum in the ε_2 function, simultaneous with a 'plasmon' mode associated with a maximum in the energy-loss function and slightly shifted to higher energies with respect to the annulation conditions of the ε_1 function.

In most practical situations, there coexist a family of n_f free electrons (with plasma frequency $\omega_p^2 = n_f e^2/m\varepsilon_0$) and one or several families of n_i bound electrons (with eigenfrequencies ω_i). The influence of bound electrons is to shift the plasma frequency towards lower values if $\omega_i > \omega_p$ and to higher values if $\omega_i < \omega_p$. As a special case, in an insulator, $n_f = 0$ and all the electrons ($n_i = n$) have a binding energy at least equal to the band gap $E_g \simeq \hbar\omega_i$, giving $\omega_p^2 = (E_g/\hbar)^2 + ne^2/m\varepsilon_0$.

This description constitutes a satisfactory first step into the world of real solids with a complex system of valence and conduction bands between which there is a strong transition rate of individual electrons under the influence of photon or electron beams. In optical spectroscopy, for instance, this transition rate, which governs the absorption coefficient, can be deduced from the calculation of the factor ε_2 as

$$\varepsilon_2(\omega) = \frac{A}{\omega^2}|M_{jj'}|^2 J_{jj'}(\omega), \qquad (4.3.4.24)$$

where $M_{jj'}$ is the matrix element for the transition from the occupied level j in the valence band to the unoccupied level j' in the conduction band, both with the same $\mathbf{k}$ value (which means for a vertical transition). $J_{jj'}(\omega)$ is the joint density of states (JDOS) with the energy difference $\hbar\omega$. This formula is also valid

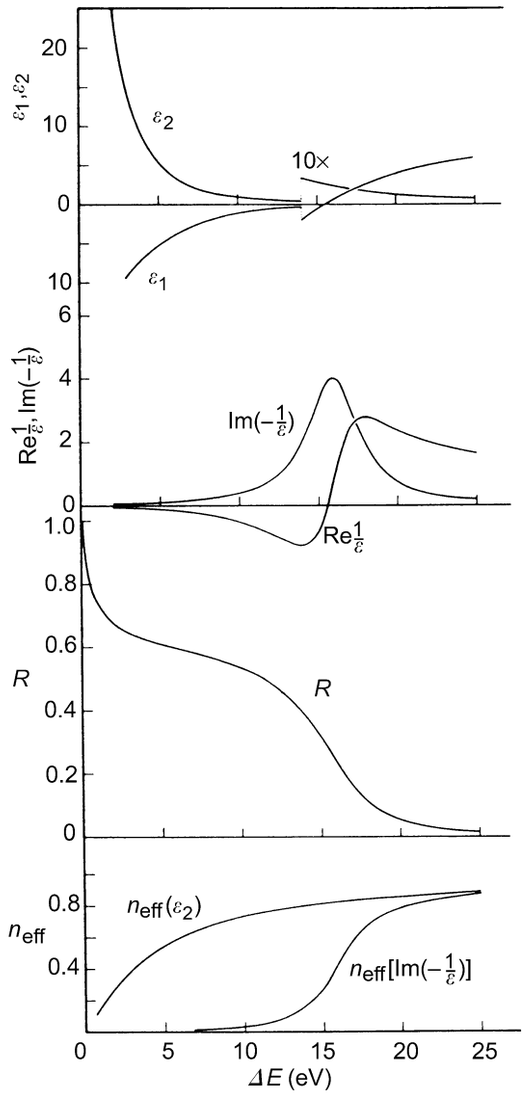

Fig. 4.3.4.16. Dielectric and optical functions calculated in the Drude model of a free-electron gas with $\hbar\omega_p = 16\,\mathrm{eV}$ and $\tau = 1.64 \times 10^{-16}\,\mathrm{s}$. R is the optical reflection coefficient in normal incidence, *i.e.* $R = [(n-1)^2 + k^2]/[(n+1)^2 + k^2]$ with n and k the real and imaginary parts of $\sqrt{\varepsilon}$. The effective numbers $n_{\mathrm{eff}}(\varepsilon_2)$ and $n_{\mathrm{eff}}[\mathrm{Im}(-1/\varepsilon)]$ are defined in Subsection 4.3.4.5 [courtesy of Daniels *et al.* (1970)].

for small-angle-scattering electron inelastic processes. When parabolic bands are used to represent, respectively, the upper part of the valence band and the lower part of the conduction band in a semiconductor, the dominant JDOS term close to the onset of the interband transitions takes the form

$$\text{JDOS} \propto (E - E_g)^{1/2}, \tag{4.3.4.25}$$

where E_g is the band-gap energy. This concept has been successfully used by Batson (1987) for the detection of gap energy variations between the bulk and the vicinity of a single misfit dislocation in a GaAs specimen. The case of non-vertical transitions involving integration over **k**-space has also been considered (Fink *et al.*, 1984; Fink & Leising, 1986).

4.3.4.3.3. *Real solids*

The dielectric constants of many solids have been deduced from a number of methods involving either primary photon or electron beams. In optical measurements, one obtains the values of ε_1 and ε_2 from a Krakers–Kronig analysis of the optical absorption and reflection curves, while in electron energy-loss measurements they are deduced from Kramers–Kronig analysis of energy-loss functions.

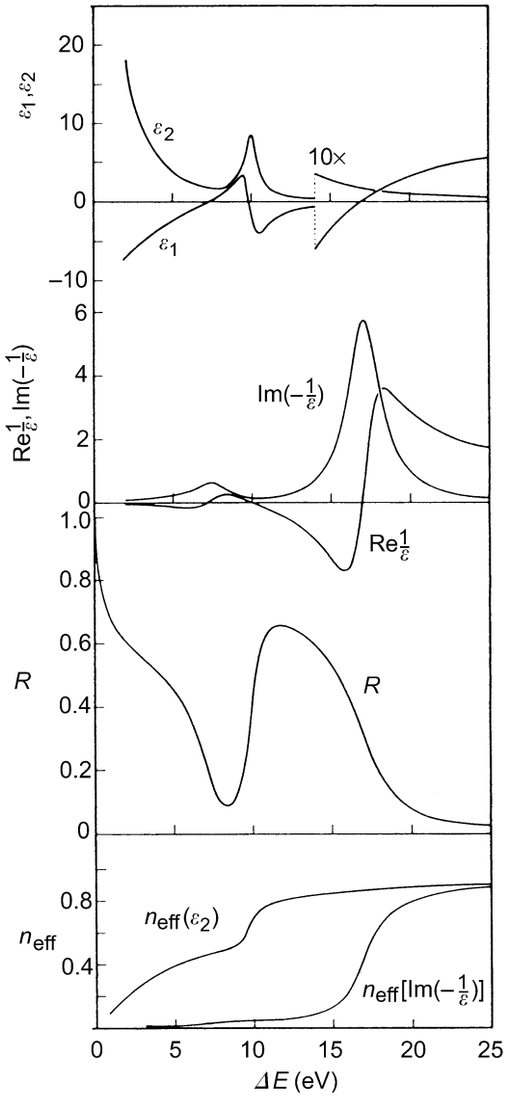

Fig. 4.3.4.17. Same as previous figure, but for a Lorentz model with an oscillator of eigenfrequency $\hbar\omega_0 = 10\,\text{eV}$ and relaxation time $\tau_0 = 6.6 \times 10^{-16}\,\text{s}$ superposed on the free-electron term [courtesy of Daniels *et al.* (1970)].

Fig. 4.3.4.18 shows typical behaviours of the dielectric and energy-loss functions.

(*a*) For a free-electron metal (Al), the Drude model is a satisfactory description with a well defined narrow and intense maximum of $\text{Im}(-1/\varepsilon)$ corresponding to the collective plasmon excitation together with typical conditions $\varepsilon_1 \simeq \varepsilon_2 \simeq 0$ for this energy $\hbar\omega_p$. One also notices a weak interband transition below 2 eV.

(*b*) For transition and noble metals (such as Au), the results strongly deviate from the free-electron gas function as a consequence of intense interband transitions originating mostly from the partially or fully filled *d* band lying in the vicinity of, or just below, the Fermi level. There is no clear condition for satisfying the criterion of plasma excitation ($\varepsilon = 0$) so that the collective modes are strongly damped. However, the higher-lying peak is more generally of a collective nature because it coincides with the exhaustion of all oscillator strengths for interband transitions.

(*c*) Similar arguments can be developed for a semiconductor (InSb) or an insulator (Xe solid). In the first case, one detects a few interband transitions at small energies that do not prevent the occurrence of a pronounced volume plasmon peak rather similar to the free-electron case. The difference between the gap and the plasma energy is so great that the valence electrons behave collectively as an assembly of free particles. In contrast, for wide gap insulators (alkali halides, oxides, solid rare gases), a number of peaks are seen, owing to different interband transitions and exciton peaks. Excitons are quasi-particles consisting of a conduction-band electron and a valence-band hole bound to each other by Coloumb interaction. One observes the existence of a band gap [no excitation either in ε_2 or in $\text{Im}(-1/\varepsilon)$ below a given critical value E_g] and again the higher-lying peak is generally of a rather collective nature.

Čerenkov radiation is emitted when the velocity v of an electron travelling through a medium exceeds the speed of light for a particular frequency in this medium. The criterion for Čerenkov emission is

$$\varepsilon_1(\omega) > \frac{c^2}{v^2} = \beta^{-2}. \tag{4.3.4.26}$$

In an insulator, ε_1 is positive at low energies and can considerably exceed unity, so that a 'radiation peak' can be detected in the corresponding energy-loss range (between 2 and 4 eV in Si, Ge, III–V compounds, diamond, ...); see Von Festenberg (1968), Kröger (1970), and Chen & Silcox (1971). The associated scattering angle, $\theta \simeq \lambda_{\text{el}}/\lambda_{\text{ph}} \simeq 10^{-5}\,\text{rad}$ for high-energy electrons, is very small and this contribution can only be detected using a limited forward-scattering angular acceptance.

In an *anisotropic* crystal, the dielectric function has the character of a tensor, so that the energy-loss function is expressed as

$$\text{Im}\left(-\frac{1}{\sum_i \sum_j \varepsilon_{ij}\, q_i\, q_j}\right). \tag{4.3.4.27}$$

If it is transformed to its orthogonal principal axes $(\varepsilon_{11}, \varepsilon_{22}, \varepsilon_{33})$, and if the **q** components in this system are q_1, q_2, q_3, the above expression simplifies to

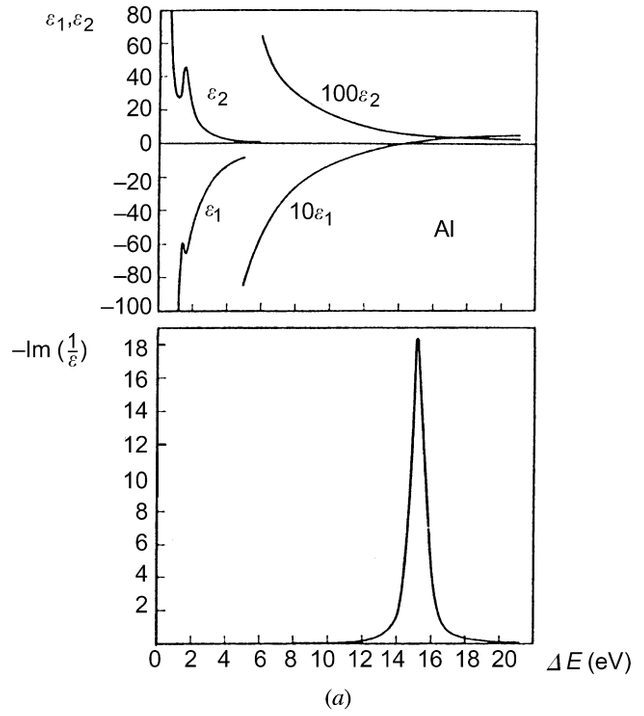

(a)

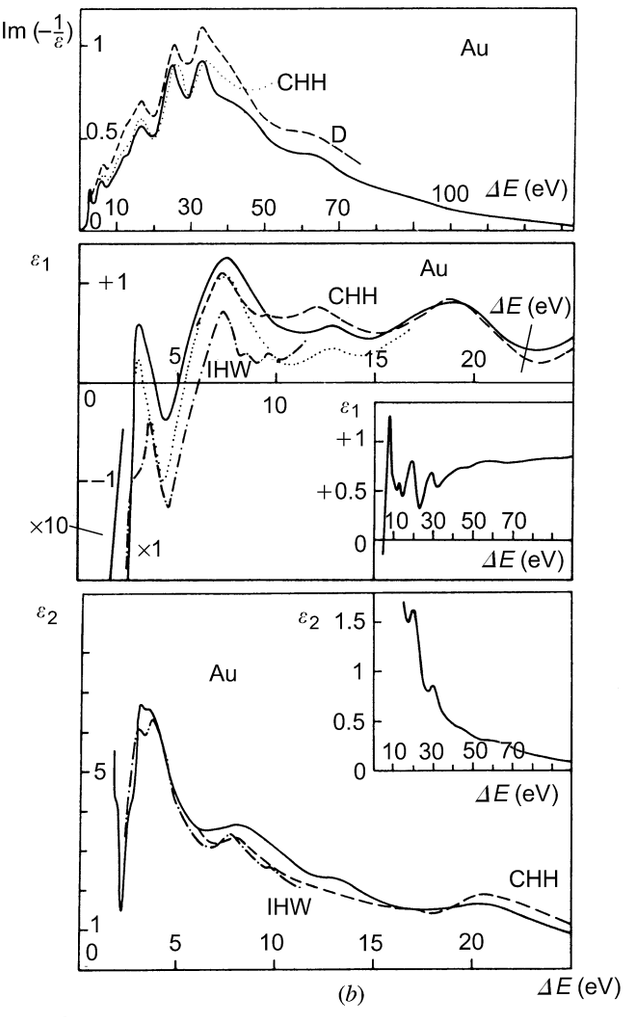

(b)

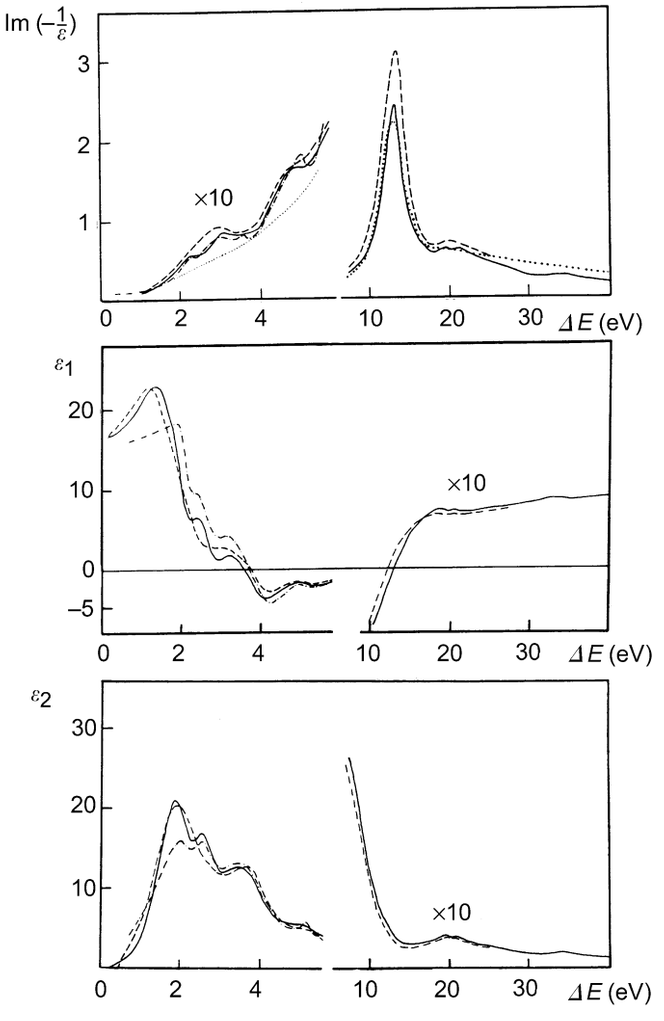

(c)

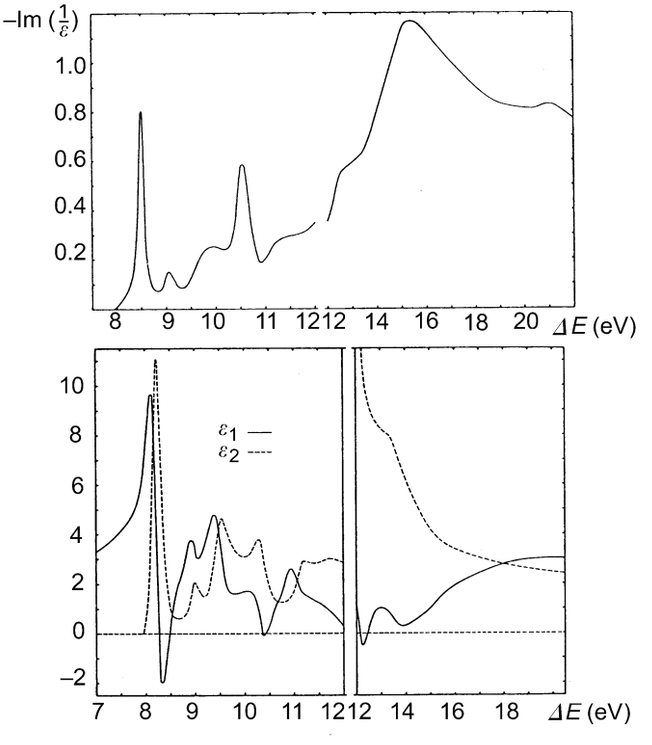

(d)

Fig. 4.3.4.18. Dielectric coefficients ε_1, ε_2 and $\mathrm{Im}(-1/\varepsilon)$ from a collection of typical real solids: (*a*) aluminium [courtesy of Raether (1965)]; (*b*) gold [courtesy of Wehenkel (1975)]; (*c*) InSb [courtesy of Zimmermann (1976)]; (*d*) solid xenon at *ca* 5 K [courtesy of Keil (1968)].

$$\mathrm{Im}\left(-\frac{1}{\sum_i \varepsilon_{ii} q_i^2}\right). \qquad (4.3.4.28)$$

In a uniaxial crystal, such as a graphite, $\varepsilon_{11} = \varepsilon_{22} = \varepsilon_\perp$ and $\varepsilon_{33} = \varepsilon_\parallel$ (*i.e.* parallel to the c axis):

$$\varepsilon(\mathbf{q}, \omega) = \varepsilon_\perp \sin^2\theta + \varepsilon_\parallel \cos^2\theta, \qquad (4.3.4.29)$$

where θ is the angle between $\mathbf{q}$ and the c axis. The spectrum depends on the direction of $\mathbf{q}$, either parallel or perpendicular to the c axis, as shown in Fig. 4.3.4.19 from Venghaus (1975). These experimental conditions may be achieved by tilting the graphite layer at 45° with respect to the incident axis, and recording spectra in two directions at $\pm\theta_E$ with respect to it (see Fig. 4.3.4.20).

4.3.4.3.4. *Surface plasmons*

Volume plasmons are longitudinal waves of charge density propagating through the bulk of the solid. Similarly, three exist longitudinal waves of charge density travelling along the surface between two media A and B (one may be a vacuum): these are the surface plasmons (Kliewer & Fuchs, 1974). Boundary conditions imply that

$$\varepsilon_A(\omega) + \varepsilon_B(\omega) = 0. \qquad (4.3.4.30)$$

The corresponding charge-density fluctuation is contained within the (**x**) boundary plane, z being normal to the surface:

$$\rho(\mathbf{x}, z) \simeq \cos(\mathbf{q}\cdot\mathbf{x} - \omega t)\delta(z), \qquad (4.3.4.31)$$

and the associated electrostatic potential oscillates in space and time as

$$\varphi(\mathbf{x}, z)\, \alpha \cos(\mathbf{q}\cdot\mathbf{x} - \omega t)\exp(-q|z|). \qquad (4.3.4.32)$$

The characteristic energy ω_s of this surface mode is estimated in the free electron case as:

In the planar interface case:

$$\left.\begin{aligned}
&\omega_s = \frac{\omega_p}{\sqrt{2}} \\
&\quad \text{(interface metal–vacuum);} \\
&\omega_s = \frac{\omega_p}{(1+\varepsilon_d)^{1/2}} \\
&\quad \text{(interface metal–dielectric of constant } \varepsilon_d\text{);} \\
&\omega_s = \left(\frac{\omega_{p_A}^2 + \omega_{p_B}^2}{2}\right)^{1/2} \\
&\quad \text{(interface metal } A\text{–metal } B\text{).}
\end{aligned}\right\} \qquad (4.3.4.33)$$

In the spherical interface case:

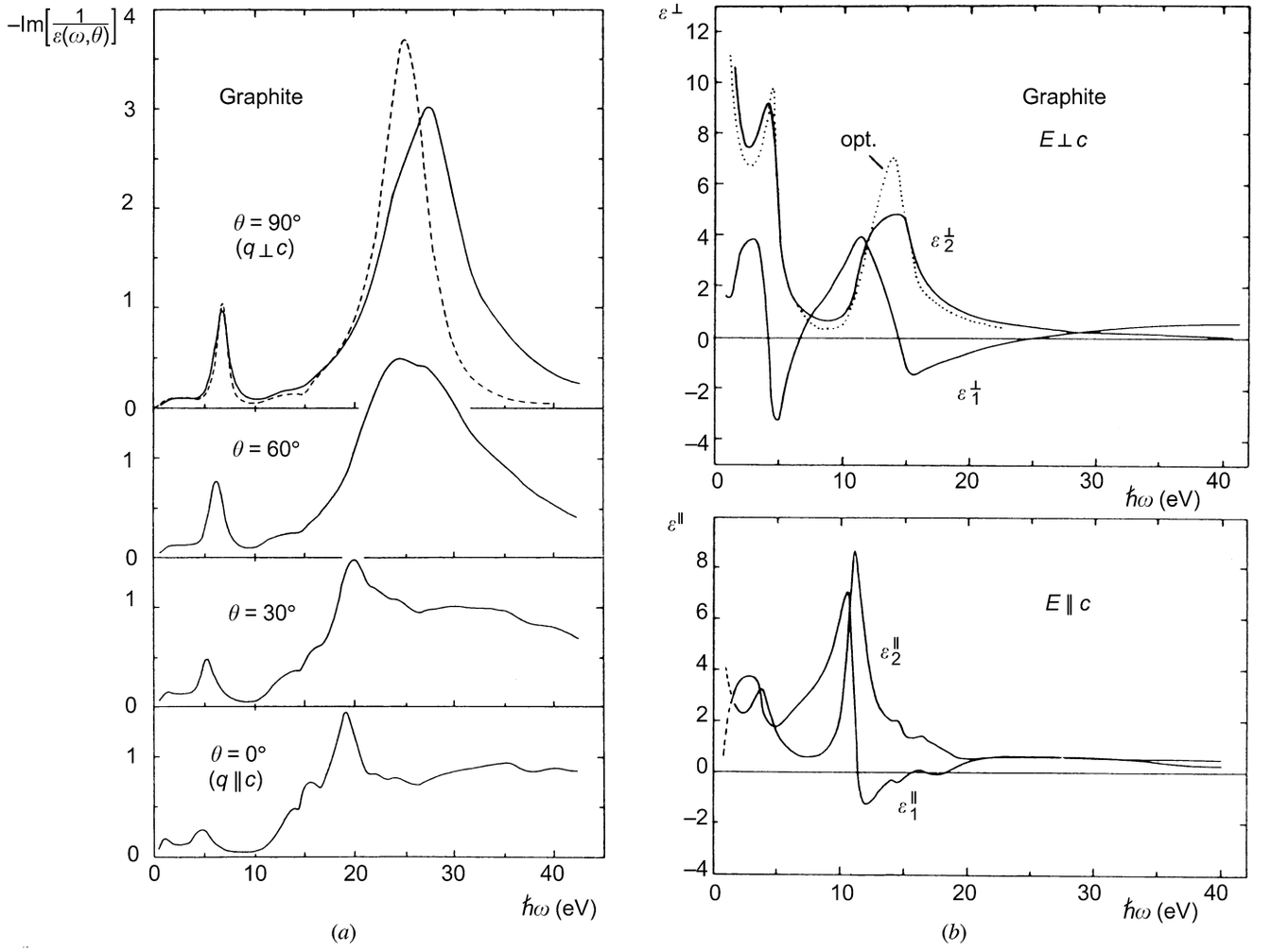

Fig. 4.3.4.19. Dielectic functions in graphite derived from energy losses for $E \perp c$ (*i.e.* the electric field vector being in the layer plane) and for $E \| c$ [from Daniels *et al.* (1970)]. The dashed line represents data extracted from optical reflectivity measurements [from Taft & Philipp (1965)].

$$(\omega_s)_l = \frac{\omega_p}{[(2l+1)/l]^{1/2}} \qquad (4.3.4.34a)$$

(metal sphere in vacuum – the modes are now quantified following the l quantum number in spherical geometry);

$$(\omega_s)_l = \frac{\omega_p}{[(2l+1)/(l+1)]^{1/2}} \qquad (4.3.4.34b)$$

(spherical void within metal).

Thin-film geometry:

$$(\omega_s)^{\pm} = \omega_p \left[\frac{1 \pm \exp(-qt)}{1+\varepsilon_d}\right]^{1/2} \qquad (4.3.4.35)$$

(metal layer of thickness t embedded in dielectric films of constant ε_d). The two solutions result from the coupling of the oscillations on the two surfaces, the electric field being symmetric for the $(\omega_s)^-$ mode and antisymmetric for the $(\omega_s)^+$.

In a real solid, the surface plasmon modes are determined by the roots of the equation $\varepsilon(\omega_s) = -1$ for vacuum coating [or $\varepsilon(\omega_s) = -\varepsilon_d$ for dielectric coating].

The probability of surface-loss excitation P_s is mostly governed by the $\mathrm{Im}\{-1/[1+\varepsilon(\omega)]\}$ energy-loss function, which is analogous for surface modes to the bulk $\mathrm{Im}\{-1/[\varepsilon(\omega)]\}$ energy-loss function. In normal incidence, the differential scattering cross section $\mathrm{d}P_s/\mathrm{d}\Omega$ is zero in the forward direction, reaches a maximum for $\theta = \pm\theta_E/3^{1/2}$, and decreases as θ^{-3} at large angles. In non-normal incidence, the angular distribution is asymmetrical, goes through a zero value for momentum transfer $\hbar\mathbf{q}$ in a direction perpendicular to the interface, and the total probability increases as

$$P_s(\varphi) = \frac{P_s(O)}{\cos\varphi}, \qquad (4.3.4.36)$$

where φ is the incidence angle between the primary beam and the normal to the surface. As a consequence, the probability of producing one (and several) surface losses increases rapidly for grazing incidences.

4.3.4.4. *Excitation spectrum of core electrons*

4.3.4.4.1. *Definition and classification of core edges*

As for any core-electron spectroscopy, EELS spectroscopy at higher energy losses mostly deals with the excitation of well defined atomic electrons. When considering solid specimens, both initial and final states in the transition are actually eigenstates in the solid state. However, the initial wavefunction can be considered as purely atomic for core excitations. As a first consequence, one can classify these transitions as a function of the parameters of atomic physics: Z is the atomic number of the element; n, l, and $j = l + s$ are the quantum numbers describing the subshells from which the electron has been excited. The spectroscopy notation used is shown in Fig. 4.3.4.21. The list of major transitions is displayed as a function of Z and E_c in Fig. 4.3.4.22.

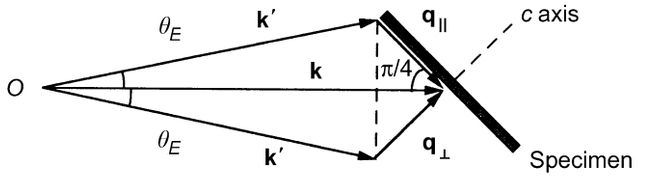

Fig. 4.3.4.20. Geometric conditions for investigating the anisotropic energy-loss function.

Core excitations appear as edges superimposed, from the threshold energy E_c upwards, above a regularly decreasing background. As explained below, the basic matrix element governing the probability of transition is similar for optical absorption spectroscopy and for small-angle-scattering EELS spectroscopy. Consequently, selection rules for dipole transitions define the dominant transitions to be observed, *i.e.*

$$l' - l = \Delta l = \pm 1 \quad \text{and} \quad j' - j = \Delta j = 0, \pm 1. \qquad (4.3.4.37)$$

This major rule has important consequences for the edge shapes to be observed: approximate behaviours are also shown in Fig. 4.3.4.22. A very useful library of core edges can be found in the EELS atlas (Ahn & Krivanek, 1982), from which we have selected the family of edges gathered in Fig. 4.3.4.23. They display the following typical profiles:

(i) *K edges for low-Z elements* ($3 \leq Z \leq 14$). The carbon K edge occurring at 284 eV is a nice example with a clear hydrogenic or saw-tooth profile and fine structures on threshold depending on the local environment (amorphous, graphite, diamond, organic molecules, ...); see Isaacson (1972*a*,*b*).

(ii) *$L_{2,3}$ edges for medium-Z elements* ($11 \lesssim Z \lesssim 45$). The $L_{2,3}$ edges exhibit different shapes when the outer occupied shell changes in nature: a delayed profile is observed as long as the first vacant d states are located, along the energy scale, rather above the Fermi level (sulfur case). When these d states coincide with the first accessible levels, sharp peaks, generally known as 'white lines', appear at threshold (this is the case for transition elements with the Fermi level inside the d band). These lines are generally split by the spin-orbit term on the initial level into $2p^{3/2}$ and $2p^{1/2}$ (or L_3 and L_2) terms. For higher-Z elements, the bound d levels are fully occupied, and

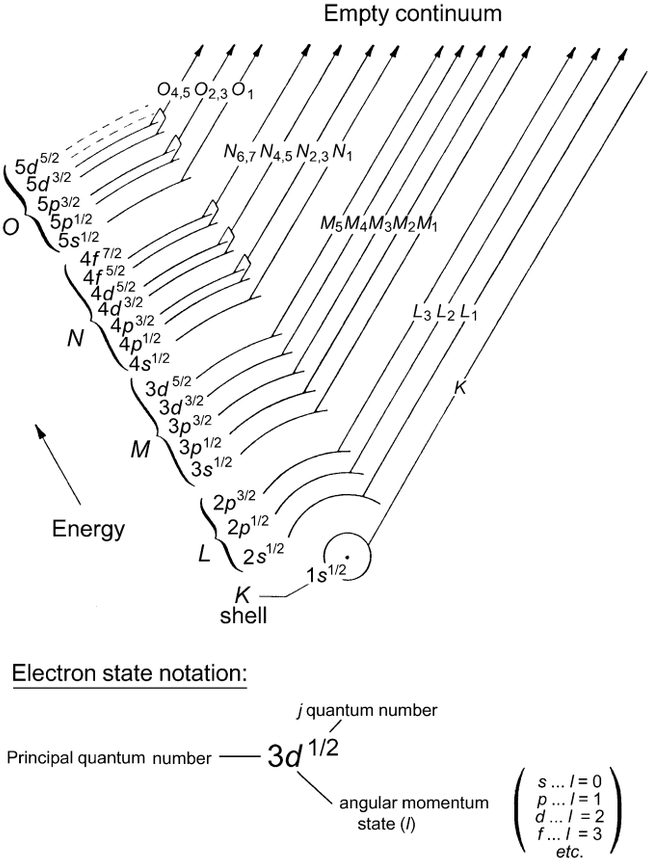

Fig. 4.3.4.21. Definition of electron shells and transitions involved in core-loss spectroscopy [from Ahn & Krivanek (1982)].

references